

## Contents lists available at ScienceDirect

# NeuroImage

journal homepage: www.elsevier.com/locate/neuroimage



# Comparative analysis of signal models for microscopic fractional anisotropy estimation using q-space trajectory encoding



Leevi Kerkelä<sup>a,\*</sup>, Fabio Nery<sup>a</sup>, Ross Callaghan<sup>b</sup>, Fenglei Zhou<sup>b,c</sup>, Noemi G. Gyori<sup>b,a</sup>, Filip Szczepankiewicz<sup>d,e,f</sup>, Marco Palombo<sup>b</sup>, Geoff J.M. Parker<sup>b,g,h</sup>, Hui Zhang<sup>b</sup>, Matt G. Hall<sup>a,i</sup>, Chris A. Clark<sup>a</sup>

- <sup>a</sup> UCL Great Ormond Street Institute of Child Health, University College London, London, UK
- <sup>b</sup> UCL Centre for Medical Image Computing, University College London, London, UK
- <sup>c</sup> UCL School of Pharmacy, University College London, London, UK
- d Department of Radiology, Brigham and Women's Hospital, Boston, Massachusetts, US
- <sup>e</sup> Harvard Medical School, Boston, Massachusetts, US
- f Clinical Sciences Lund, Lund University, Lund, Sweden
- g Bioxydyn Limited, Manchester, UK
- h UCL Queen Square Institute of Neurology, University College London, London, UK
- <sup>i</sup> National Physical Laboratory, Teddington, UK

#### ARTICLE INFO

#### ABSTRACT

Keywords:
Diffusion MRI
Microscopic fractional anisotropy
Multidimensional diffusion encoding
Signal model

Microscopic diffusion anisotropy imaging using diffusion-weighted MRI and multidimensional diffusion encoding is a promising method for quantifying clinically and scientifically relevant microstructural properties of neural tissue. Several methods for estimating microscopic fractional anisotropy (µFA), a normalized measure of microscopic diffusion anisotropy, have been introduced but the differences between the methods have received little attention thus far. In this study, the accuracy and precision of µFA estimation using q-space trajectory encoding and different signal models were assessed using imaging experiments and simulations. Three healthy volunteers and a microfibre phantom were imaged with five non-zero b-values and gradient waveforms encoding linear and spherical b-tensors. Since the ground-truth μFA was unknown in the imaging experiments, Monte Carlo random walk simulations were performed using axon-mimicking fibres for which the ground truth was known. Furthermore, parameter bias due to time-dependent diffusion was quantified by repeating the simulations with tuned waveforms, which have similar power spectra, and with triple diffusion encoding, which, unlike q-space trajectory encoding, is not based on the assumption of time-independent diffusion. The truncated cumulant expansion of the powder-averaged signal, gamma-distributed diffusivities assumption, and q-space trajectory imaging, a generalization of the truncated cumulant expansion to individual signals, were used to estimate μFA. The gammadistributed diffusivities assumption consistently resulted in greater µFA values than the second order cumulant expansion, 0.1 greater when averaged over the whole brain. In the simulations, the generalized cumulant expansion provided the most accurate estimates. Importantly, although time-dependent diffusion caused significant overestimation of μFA using all the studied methods, the simulations suggest that the resulting bias in μFA is less than 0.1 in human white matter.

#### 1. Introduction

Diffusion-weighted magnetic resonance imaging (dMRI) has become firmly established as the MRI technique of choice for quantify-

E-mail address: leevi.kerkela.17@ucl.ac.uk (L. Kerkelä).

Abbreviations: CV, coefficient of variation; ConFiG, contextual fibre growth; DDE, double diffusion encoding; dMRI, diffusion-weighted magnetic resonance imaging; DTD, diffusion tensor distribution; DTI, diffusion tensor imaging; FA, fractional anisotropy; FOV, field of view; GPU, graphical processing unit; IQR, interquartile range; LTE, linear tensor encoding; MD, mean diffusivity; MDE, multidimensional diffusion encoding; MSE, mean squared error; μFA, microscopic fractional anisotropy; ROI, region of interest; SDE, single diffusion encoding; SNR, signal-to-noise ratio; STE, spherical tensor encoding; TDE, triple diffusion encoding; TE, echo time; TR, repetition time; QTE, q-space trajectory encoding; QTI, q-space trajectory imaging.

<sup>\*</sup> Corresponding author. Developmental Imaging & Biophysics Section, UCL Great Ormond Street Institute of Child Health, 30 Guilford Street, WC1N 1EH, London, UK.

L. Kerkelä, F. Nery, R. Callaghan et al. NeuroImage 242 (2021) 118445

ing neural tissue's microstructural properties in vivo (Johansen-Berg and Behrens, 2013). Since the pioneering work by Basser et al. (1994), diffusion tensor imaging (DTI) parameters quantifying the magnitude and shape of the voxel-level diffusion tensor have been widely applied in characterizing brain development and pathologies (Assaf et al., 2019). Despite its utility, DTI suffers from various well-recognized limitations that have been addressed by the subsequent advances in the field. Because orientation dispersion of anisotropic neurites can result in an isotropic diffusion tensor, several methods have been developed to obtain a more accurate estimate of the fibre orientation distribution, e.g., (Tournier et al., 2007; Tuch, 2004; Wedeen et al., 2008). Another major limitation of DTI is that it does not provide a good fit to data in experiments with moderate to high diffusion-weighting (roughly  $b < ms/\mu m^2$ in the brain) when the signal as a function of b-value clearly deviates from a monoexponential decay, revealing that the voxel-level diffusion propagator is not Gaussian, especially in white matter (Jensen et al., 2005). More complicated signal models capturing the deviation from the monoexponential decay, e.g., (Clark et al., 2002; Jensen et al., 2005; Novikov and Kiselev, 2010), as well as a plenitude of microstructural models, e.g., (Jespersen et al., 2007; Sotiropoulos et al., 2012; Zhang et al., 2012), have been developed to obtain a better fit to data and additional information on tissue microstructure. Comprehensive overviews of the state of the field are provided by Jelescu and Budde (2017) and Novikov et al. (2019), for example.

The methods referred to above belong to a class of single diffusion encoding (SDE) methods (Shemesh et al., 2016) as they are based on acquisitions measuring the displacements of water molecules along a single dimension, i.e., the direction of the diffusion encoding magnetic field gradient. Despite being sensitive to several microstructural changes, SDE methods are fundamentally limited because they confound two major sources of voxel-level non-Gaussian diffusion, namely, the orientation dispersion of anisotropic diffusion and the size variance of microscopic diffusion environments, resulting in a lack of specificity (Westin et al., 2016). This fundamental degeneracy of SDE acquisitions also prevents accurate measurement of microscopic diffusion anisotropy without substantial a priori information about tissue microstructure (Henriques et al., 2019; Ianuş et al., 2016; Lampinen et al., 2017). Multidimensional diffusion encoding (MDE), on the other hand, renders the dMRI signal sensitive to the displacements of water molecules along two or three dimensions. Over recent years, MDE methods, such as double diffusion encoding (DDE) and q-space trajectory encoding (QTE), have gained significant attention for their ability to resolve the fundamental degeneracy in data acquired with conventional SDE methods, capturing clinically and scientifically relevant information about tissue microstructure (Cory et al., 1990; Eriksson et al., 2013; Henriques et al., 2020b; Jespersen et al., 2013; Lasič et al., 2014; Mitra, 1995; Topgaard, 2017; Westin et al., 2016).

DDE waveforms consist of two trapezoidal pulse pairs separated by a mixing time and therefore require rather long echo times, resulting in a diminished signal. Using clinical whole-body scanners, asymmetric DDE waveforms can also produce significant concomitant gradients in spin echo experiments, causing artefacts and signal dropout (Szczepankiewicz et al., 2019c), an issue that can be avoided by using double spin echo (Koch and Finsterbusch, 2008). QTE waveforms are designed to enable spin echo experiments with shorter echo times by following an optimized trajectory in q-space to define a b-tensor with the desired shape, orientation, and magnitude (Sjölund et al., 2015). This makes it feasible to perform MDE experiments using more limited scanner hardware (Szczepankiewicz et al., 2019b), albeit at the cost of assuming diffusion time dependency to be negligible because QTE waveforms lack a well-defined scalar diffusion time. If this assumption is not valid, a discrepancy between the diffusion times of the gradient waveforms encoding different b-tensors shapes results in biased parameter estimates, as shown by Lundell et al. (2019, 2017), who proposed reducing the bias by using so-called tuned waveforms with similar power spectra at least along one direction. Furthermore, isotropic diffusion encoding with QTE may be orientationally variant due to significant time-dependent microscopic diffusion anisotropy (Jespersen et al., 2019; de Swiet and Mitra, 1996).

By combining MDE acquisitions with different b-tensor shapes, it is possible to estimate microscopic diffusion anisotropy, i.e., the average anisotropy of the microscopic diffusion environments, referred to as compartments hereafter, irrespective of their orientation dispersion. Since microscopic diffusion anisotropy does not depend on the orientation dispersion of axons, it may be a clinically valuable biomarker for axonal degeneration. Indeed, promising results of the application of microscopic fractional anisotropy (µFA) (Lasič et al., 2014), a normalized measure of microscopic diffusion anisotropy that is equivalent to conventional fractional anisotropy (FA) if the compartments are aligned, have been reported in imaging brain tumours (Szczepankiewicz et al., 2015; 2016), multiple sclerosis lesions (Andersen et al., 2020; Yang et al., 2018), and microstructural properties of white matter associated with schizophrenia (Westin et al., 2016), epilepsy (Lampinen et al., 2020), and aging and Parkinson's disease (Kamiya et al., 2020). However, different studies have applied different methods for estimating µFA and the differences between the methods have received little attention thus far. Understanding how different µFA estimation methods relate to each other is crucial in planning future studies and interpreting previously reported results. Furthermore, reaching a consensus on the optimal method for measuring µFA is an essential requirement for future clinical studies.

In this study, imaging experiments and simulations were performed to compare the accuracy and precision of µFA estimation using the following signal models: truncated cumulant expansion of the powderaveraged signal (Ianuş et al., 2018; Jespersen et al., 2013; Lasič et al., 2014; Nery et al., 2019; Yang et al., 2018), gamma-distributed apparent diffusivities (Andersen et al., 2020; Lasič et al., 2014; Szczepankiewicz et al., 2015; 2016), and q-space trajectory imaging (QTI), a generalization of the truncated cumulant expansion to individual acquisitions using diffusion tensor distribution (DTD) as a microstructural model, (Kamiya et al., 2020; Lampinen et al., 2020; Martin et al., 2020; Westin et al., 2016). The  $\mu FA$  maps in healthy volunteers calculated from the same data using the different methods were compared. The precision of the estimates was quantified by repeatedly imaging a microfibre phantom. Furthermore, since the ground-truth value of µFA was unknown in the imaging experiments, Monte Carlo random walk simulations were performed using axon-mimicking fibres for which the ground truth was known. The bias in µFA due to time-dependent diffusion was quantified by repeating the simulations with tuned waveforms and with triple diffusion encoding (TDE).

#### 2. Theory

Conventional DTI represents diffusion at the voxel level by a symmetric positive definite  $3\times3$  tensor **D** that captures Gaussian diffusion (Basser et al., 1994). As the magnitude of diffusion-weighting is increased, the signal as a function of b-value starts to deviate from a monoexponential decay, revealing that the voxel-level diffusion propagator is not Gaussian, especially in white matter (Jensen et al., 2005). At the voxel level, non-Gaussian diffusion is caused by intra-compartmental restricted diffusion and variance in diffusion properties across the compartments (Henriques et al., 2020a). The theory presented in this section is based on the assumption that the effects of intra-compartmental restricted diffusion are negligible.

If inter-compartmental exchange of water and intra-compartmental diffusion time dependence are negligible, the tissue in a voxel can be represented by a distribution of microscopic diffusion tensors representing the compartments (Westin et al., 2014). In this case, the diffusion-weighted signal can be expressed as

$$S = S_0 \int P_{\rm 6D}(\mathbf{D}_{\mu}) \exp\left(-\mathbf{b} : \mathbf{D}_{\mu}\right) d\mathbf{D}_{\mu}, \tag{1}$$

where  $S_0$  is the signal without diffusion-weighting,  $\mathbf{D}_{\mu}$  is a microscopic diffusion tensor,  $P_{6\mathrm{D}}$  is the normalized distribution of microscopic diffusion tensors in the voxel,  $\mathbf{b}$  is the b-tensor used in the acquisition, : denotes the generalized scalar product ( $\mathbf{b}: \mathbf{D} = \sum_{i=1}^3 \sum_{j=1}^3 b_{ij} D_{ij}$ ), and integration is performed over all symmetric positive definite  $3\times 3$  tensors (Westin et al., 2016). QTE is based on the idea that if intracompartmental diffusion is Gaussian, the diffusion-weighted signal attenuation depends only on  $\mathbf{b}$ , assuming that all the other imaging parameters are kept constant (Westin et al., 2016).

Since recovering the six-dimensional microscopic diffusion tensor distribution is an ill-posed problem (Topgaard, 2017), several methods have been developed for estimating relevant properties of it. One of these is  $\mu$ FA, a normalized measure of the average eigenvalue variance of the microscopic diffusion tensors (Jespersen et al., 2013; Lasič et al., 2014; Szczepankiewicz et al., 2016):

$$\mu FA = \sqrt{\frac{3}{2} \frac{\left\langle Var_{\lambda}(\mathbf{D}_{\mu}) \right\rangle}{\left\langle Var_{\lambda}(\mathbf{D}_{\mu}) \right\rangle + \left\langle [Tr(\mathbf{D}_{\mu})/3]^{2} \right\rangle}},$$
(2)

where  ${\rm Var}_{\lambda}(\ )$  denotes an operator that calculates the eigenvalue variance of a tensor,  ${\rm Tr}(\ )$  denotes the trace of a tensor, and  $\langle\ \rangle$  denotes averaging over the DTD.

## 2.1. Powder-averaged signal

The powder-averaged signal, i.e., the signal averaged over all possible diffusion encoding directions, is orientationally invariant and can be expressed as

$$S = S_0 \int_0^\infty P(D_\mu) \exp(-bD_\mu) dD_\mu, \tag{3}$$

where P is the distribution of apparent microscopic diffusivities in the voxel, b is the b-value used in the acquisition, and  $D_{\mu}$  is the apparent microscopic diffusivity (Lasič et al., 2014). P depends on the shape of the b-tensor used in the acquisition. The powder-averaged signal can be accurately estimated by averaging over the acquired diffusion encoding directions, given that the signal-to-noise ratio (SNR) is high enough and a sufficient number of directions is used (Jespersen et al., 2013; Szczepankiewicz et al., 2019b).

## 2.1.1. Second order cumulant expansion

Using the cumulant expansion up to the second order in b, the powder-averaged signal can be expressed as

$$S \approx S_0 \exp\left(-b\text{MD} + b^2 \frac{V}{2}\right),$$
 (4)

where MD =  $\langle {\rm Tr}({\bf D}_{\mu})/3 \rangle$  is the voxel-level mean diffusivity and V is the second central moment, i.e., variance, of P (Lasič et al., 2014). By combining acquisitions with different b-tensor shapes, the total variance in apparent microscopic diffusivities can be decomposed into anisotropic and isotropic variances,  $V_{\rm aniso}$  and  $V_{\rm iso}$ , respectively (Szczepankiewicz et al., 2016).  $V_{\rm aniso}$  is proportional to the average eigenvalue variance of the microscopic diffusion tensors and  $V_{\rm iso}$  is equal to the variance of mean diffusivities of the microscopic diffusion tensors:

$$V_{\rm aniso} = \frac{2}{5} \langle \text{Var}_{\lambda}(\mathbf{D}_{\mu}) \rangle, \tag{5}$$

$$V_{\rm iso} = \langle [\text{Tr}(\mathbf{D}_u)/3]^2 \rangle - \text{MD}^2. \tag{6}$$

In experiments with linear and spherical b-tensors, such as in this study, the total variance relates to anisotropic and isotropic variances as

$$V_{\rm LTE} = V_{\rm aniso} + V_{\rm iso},\tag{7}$$

$$V_{\text{STE}} = V_{\text{iso}},\tag{8}$$

where the subscripts LTE and STE represent acquisitions with linear tensor encoding and spherical tensor encoding, respectively

(Szczepankiewicz et al., 2016). Therefore,  $\mu$ FA can be estimated by fitting a signal model, e.g, Eq. (4), to the estimated powder-averaged signals acquired with linear and spherical b-tensors.

#### 2.1.2. Higher-order correction

The limitation of estimating  $\mu$ FA as described above is that Eq. (4) is strictly valid as  $b \to 0$ . However, the applied b-value has to be sufficiently high for voxel-level non-Gaussian diffusion to be measurable. The accuracy of  $\mu$ FA estimation using the truncated cumulant expansion and DDE has been shown to improve if an additional term is introduced to account for higher-order effects (Janus et al., 2018):

$$S \approx S_0 \exp\left(-bMD + b^2 \frac{V}{2} - b^3 P_3\right),\tag{9}$$

where  $P_3 \in \mathbb{R}$ . This correction, which is applied to the signal model representing acquisitions with linear encoding, was introduced to correct for higher-order effects in the difference between the signals acquired with different b-tensor shapes. It can reduce the b-value-dependent underestimation of  $\mu$ FA (Ianus et al., 2018).

#### 2.1.3. Gamma-distributed apparent diffusivities

The distribution of apparent microscopic diffusivities can also be *a priori* assumed to be such that enables Eq. (3) to be analytically evaluated, e.g., gamma-distributed (Jensen and Helpern, 2010):

$$P(D_{\mu}; k, \theta) = \frac{(D_{\mu})^{k-1}}{\Gamma(k)\theta^k} \exp\left(-\frac{D_{\mu}}{\theta}\right), \tag{10}$$

where  $k \in \mathbb{R}_+$  and  $\theta \in \mathbb{R}_+$  are the shape and scale parameters of the gamma distribution, respectively, and  $\Gamma$  is the gamma function. Under this assumption, the powder-averaged signal can be expressed as

$$S \approx S_0 \left( 1 + b \frac{V}{\text{MD}} \right)^{-\frac{\text{MD}^2}{V}},\tag{11}$$

where MD =  $k\theta$  and  $V = k\theta^2$  (Lasič et al., 2014). However, the resulting parameter estimates can be inaccurate if the distribution of apparent microscopic diffusivities is not gamma-distributed.

## 2.2. Q-space trajectory imaging

The second order cumulant expansion has also been generalized to describe individual acquisitions instead of the powder-averaged signal. In QTI (Westin et al., 2016), the signal in a single acquisition is expressed as

$$S \approx S_0 \exp\left(-\mathbf{b} : \mathbf{D} + \frac{1}{2}(\mathbf{b} \otimes \mathbf{b}) : \mathbb{C}\right),$$
 (12)

where  $\otimes$  denotes the tensor outer product and  $\mathbb C$  is a  $3\times 3\times 3\times 3$  covariance tensor defined as

$$\mathbb{C} = \langle \mathbf{D}_{u} \otimes \mathbf{D}_{u} \rangle - \mathbf{D} \otimes \mathbf{D}. \tag{13}$$

The covariance tensor contains 21 unique elements and enables the estimation of several relevant properties of the DTD.  $\mu FA$  can be calculated as

$$\mu FA = \sqrt{\frac{3}{2} \frac{\langle \mathbf{D}_{\mu} \otimes \mathbf{D}_{\mu} \rangle : \mathbb{E}_{\text{shear}}}{\langle \mathbf{D}_{\mu} \otimes \mathbf{D}_{\mu} \rangle : \mathbb{E}_{\text{iso}}}},$$
(14)

where  $\mathbb{E}_{iso}$  and  $\mathbb{E}_{shear}$  are the isotropic and shear tensors of rank 2 and shape  $6\times 6$  as described by Westin et al. (2016).

#### 3. Methods

#### 3.1. µFA estimation

Four signal models for  $\mu$ FA estimation were compared: the cumulant expansion of the powder-averaged signal up to the second order in b (Eq. (4)) and with a higher-order correction (Eq. (9)), the gamma-distributed diffusivities assumption (Eq. (11)), and QTI (Eq. (12)). For

brevity, the methods will be referred to hereafter as the cumulant model, higher-order model, gamma model, and QTI.

The powder-averaged signal was estimated by averaging over the acquired diffusion encoding directions. The cumulant model, higher-order model, and gamma model were fit to the estimated powder-averaged signal using a non-linear least squares trust region reflective algorithm (Branch et al., 1999) in Scipy (Virtanen et al., 2020).  $S_0$ , MD,  $V_{\rm aniso}$ ,  $V_{\rm iso}$ , and  $P_3$  were used as fit parameters from which  $\mu \rm FA$  was estimated using Eqs. (2), (5), and (6). The fit parameters were constrained to be non-negative real numbers. The initial values of the fit parameters were:  $S_0$  = average signal over acquisitions without diffusion-weighting, MD = 1  $\mu \rm m^2/ms$ ,  $V_{\rm aniso}$  = 0.1  $\mu \rm m^4/ms^2$ ,  $V_{\rm iso}$  = 0.1  $\mu \rm m^4/ms^2$ , and  $P_3$  = 0. QTI was fit to data using the following linear equation:

$$\boldsymbol{\beta} = (\mathbf{X}^{\mathrm{T}}\mathbf{C}\mathbf{X})^{-1}(\mathbf{X}^{\mathrm{T}}\mathbf{C})\mathbf{S},\tag{15}$$

where

$$\boldsymbol{\beta} = \begin{pmatrix} \ln S_0 & \mathbf{D} & \mathbb{C} \end{pmatrix}^{\mathrm{T}},\tag{16}$$

$$\mathbf{X} = \begin{pmatrix} 1 & -\mathbf{b}_{1}^{\mathrm{T}} & \frac{1}{2}(\mathbf{b}_{1} \otimes \mathbf{b}_{1})^{\mathrm{T}} \\ \vdots & \vdots & \vdots \\ 1 & -\mathbf{b}_{n}^{\mathrm{T}} & \frac{1}{2}(\mathbf{b}_{n} \otimes \mathbf{b}_{n})^{\mathrm{T}} \end{pmatrix}, \tag{17}$$

$$\mathbf{S} = \begin{pmatrix} \ln S_1 \\ \vdots \\ \ln S_n \end{pmatrix},\tag{18}$$

where n is the number of acquisitions and  $\mathbf{D}$ ,  $\mathbb{C}$ ,  $\mathbf{b}_i$ , and  $(\mathbf{b}_i \otimes \mathbf{b}_i)$  are column vectors in Voigt notation (Westin et al., 2016). The diagonal matrix  $\mathbf{C}$  with elements  $C_{ii} = S_i$  was used to correct for heteroscedasticity in the log-transformed data (Jones and Cercignani, 2010). The matrix inversion in Eq. (15) was performed using the Moore-Penrose pseudoinversion (Strang and Borre, 1997) in Numpy (Walt et al., 2011).  $\mu$ FA was calculated according to Eqs. (13) and (14).

## 3.2. Imaging experiments

Data was acquired using a prototype spin echo sequence (Szczepankiewicz et al., 2019a) on a Siemens Magnetom Prisma 3T (Siemens Healthcare, Erlangen, Germany) with a maximum gradient strength of 80 mT/m, maximum slew rate of 200 T/m/s, and 64-channel head coil at Great Ormond Street Hospital, London, United Kingdom. Data was preprocessed with random matrix denoising (Veraart et al., 2016) and Gibbs ringing correction (Kellner et al., 2016) using MRtrix3 (Tournier et al., 2019) and distortion correction using FSL's topup and eddy (Andersson and Sotiropoulos, 2016; Jenkinson et al., 2012).

Twelve diffusion encoding directions were used for b-values 0.1, 0.5, and 1 ms/ $\mu$ m² and 32 directions for b-values 1.5 and 2 ms/ $\mu$ m². The directions were distributed uniformly around the surface of a sphere by combining the vertex coordinates of the icosahedron and dodecahedron (Westin et al., 2016). The protocol also included 15 images without diffusion-weighting, one of which had the phase encoding direction reversed. Other relevant imaging parameters were: voxel size = 2 × 2 × 2 mm³, FOV = 256 × 256 mm², TE = 103 ms, and phase partial Fourier = 6/8.

Data was acquired using numerically optimized (Sjölund et al., 2015) and Maxwell-compensated (Szczepankiewicz et al., 2019c) gradient waveforms encoding linear and spherical b-tensors (Fig. 1A-B). To avoid peripheral nerve stimulation and gradient coil heating, the slew rate was constrained to a maximum of 65 T/m/s when calculating the gradient waveforms using the software provided by Sjölund et al. (2015). The waveforms for both linear and spherical encoding were rotated according to the diffusion encoding directions (Szczepankiewicz et al., 2019a).

Under the Gaussian phase approximation, the diffusion time of a QTE gradient waveform can be quantified by calculating the power spectrum

of the corresponding wave vector (Stepišnik, 1993):

$$PSD(\omega) = \left| \int_0^{TE} q(t) \exp(-i\omega t) dt \right|^2, \tag{19}$$

where PSD stands for power spectral density, q is the wave vector magnitude along a single direction, and  $\omega$  is the diffusion frequency. The power spectra of the Cartesian components of the unrotated waveforms used in the imaging experiments are shown in Fig. 1E-F.

Since the STE waveform exhibits spectral anisotropy, which may lead to an orientationally variant signal (Jespersen et al., 2019), the orientational variance of the STE acquisition was quantified using the correlation between the FA values estimated from LTE and STE data. If the STE acquisition is orientationally invariant, non-zero values of FA calculated from the STE data are caused by noise and they are uncorrelated with the FA values calculated from the LTE data. DTI was fit separately to LTE and STE data using a weighted linear least squares fit in Dipy (Garyfallidis et al., 2014).

## 3.2.1. Volunteer experiments

The experiments were approved by the UCL Research Ethics Committee. Each participants gave written and informed consent prior to the scan.

Three healthy adult volunteers (two females and one male with ages ranging from 27 to 42 years) were scanned with whole-brain coverage and the following imaging parameters: 60 slices, TR = 10 s, and 2 repetitions. The total scan time was approximately 40 minutes per volunteer. Areas of cerebrospinal fluid were excluded from the analysis by excluding the voxels where MD > 2.5  $\mu m^2/ms$ .

The agreement between the  $\mu$ FA maps was quantified using the concordance correlation coefficient  $\rho_c$  (Lin, 1989), which quantifies the agreement between two variables measuring the same quantity. The values of  $\rho_c$  range from -1 to 1, with perfect agreement at 1.

## 3.2.2. Phantom experiments

A phantom consisting of highly hydrophilic hollow polycaprolactone microfibres (Zhou et al., 2018) was imaged with the following imaging parameters: TR = 3 s, 10 slices, and 1 repetition. The phantom contained three regions of interest (ROI) with different fibre configurations: parallel fibres, perpendicularly crossing fibres, and fibres with random orientations. The inner diameter of the fibres was 9.9  $\pm$  1.2  $\mu m$  (mean  $\pm$  standard deviation) in the ROI containing parallel and crossing fibres, and 7.8  $\pm$  0.5  $\mu m$  in the ROI containing randomly oriented fibres. Scanning electron microscope images illustrating the microstructure of the phantom are shown in Fig. 2.

The acquisition protocol was repeated 11 times to study the precision of  $\mu FA$ . The coefficient of variation (CV) was calculated at each voxel as CV =  $(\sigma/\mu) \cdot 100\%$ , where  $\sigma$  is the standard deviation of  $\mu FA$  estimated using a given method over the repeated acquisitions and  $\mu$  is the mean  $\mu FA$  averaged over all acquisitions and methods. A single value of  $\mu$  was used to not penalize the methods that produce lower values of  $\mu FA$ .

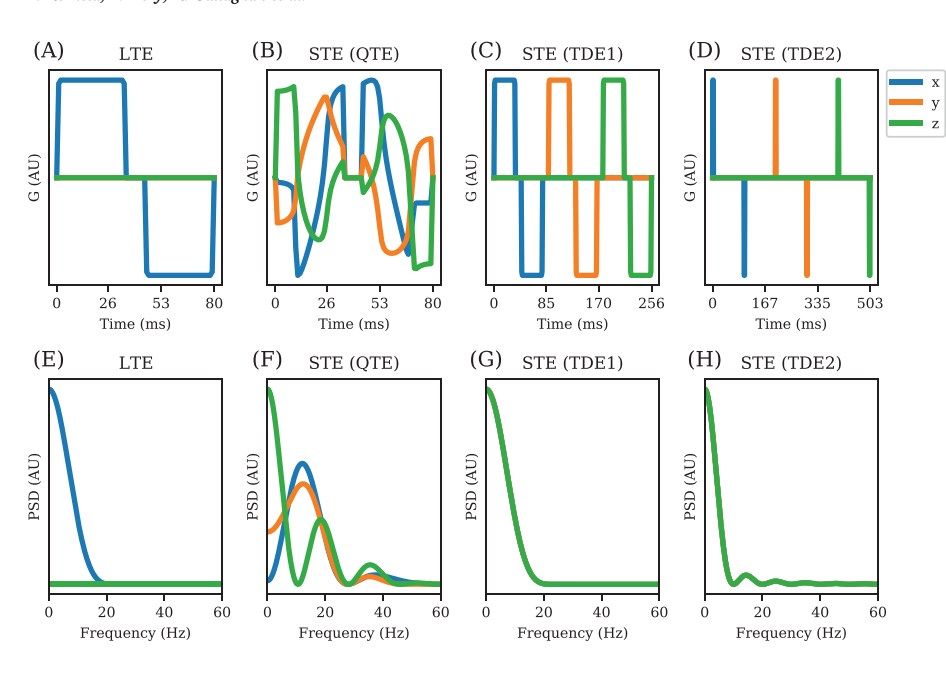
## 3.3. Simulation experiments

GPU-accelerated Monte Carlo random walk simulations were performed using Disimpy (Kerkelä et al., 2020) to compare the signal models in a scenario where the ground truth was known and to assess  $\mu FA$  bias due to time-dependent diffusion. The functionality of the simulator has been confirmed by comparing the simulated signals to analytical solutions using simple geometries, such as cylinders and spheres. Validation examples are available on the documentation (https://disimpy.readthedocs.io).

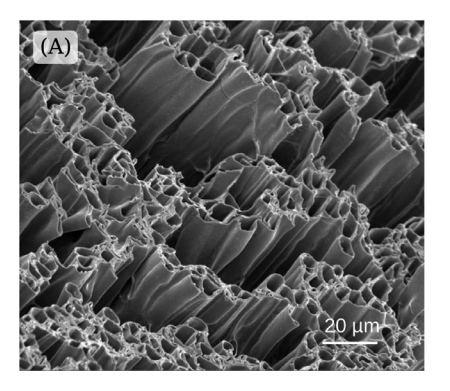
## 3.3.1. Simulated microstructure

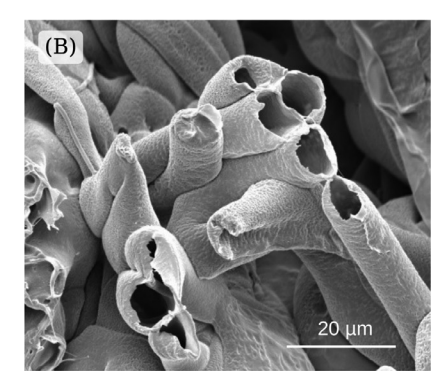
The simulated microstructure, shown in Fig. 3A, consisted of 1,713,598 triangles generated using ConFiG numerical phantom generator (Callaghan et al., 2020) to represent a white matter region with

L. Kerkelä, F. Nery, R. Callaghan et al. NeuroImage 242 (2021) 118445

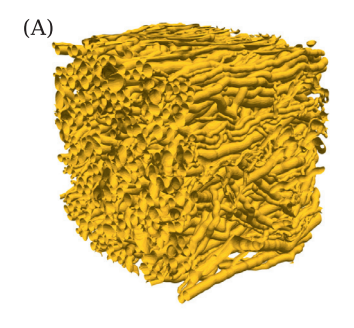


**Fig. 1.** The diffusion encoding gradient waveforms used in the imaging experiments (A-B) and simulations (A-D), and the corresponding power spectra (E-H). It is important to note that the power spectra of the unrotated triple diffusion encoding waveforms are identical along x, y and z but not along arbitrary directions.





**Fig. 2.** Representative scanning electron microscope images illustrating the microstructure of the parallel microfibres phantom (A) and the randomly oriented microfibres phantom (B). The phantom with crossing microfibres was made from the same sample as the one with parallel microfibres.



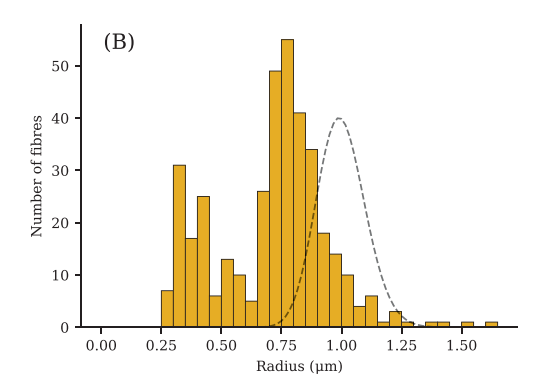


**Fig. 3.** (A) The simulated voxel containing 381 axon-mimicking fibres. (B) A histogram of the fibre radii (mean along the fibre length). The dashed line denotes the probability distribution from which the target radii where sampled. The fibre radii skew towards smaller radii than the target distribution due to the fact that as the fibres grow in ConFiG, they often have to shrink to fit into the available space.

dispersed axons. Palombo et al. (2019) have shown that the triangulation of a simulated cell membrane has a small effect on the simulated signal. The target orientation distribution of the fibres was drawn from a Watson distribution with  $\kappa=2$  (Mardia and Jupp, 2009), target radius distribution was drawn from a gamma distribution with mean of 1  $\mu m$  and standard deviation of 0.1  $\mu m$ , and target fibre density was 70%. The resulting voxel contained 381 irregular and impermeable axon-mimicking fibres at a fibre density of 60%. The fibre radii skew towards smaller radii than the target distribution, as seen in Fig. 3B, due to the fact that as the fibres grow in ConFiG, they often have to shrink to fit into the available space. Periodic boundary conditions were used, i.e., the random walkers that left the voxel encountered repeating identical

copies of the shown microstructure. To ensure that the ends of the fibres matched, cut fibres were extended with mirrored copies of themselves in the directions aligned with the main fibre direction, and the final voxel included 50% of the mirrored copies. In the plane perpendicular to the direction of the fibres, the fibres were grown in a way that ensures periodicity. The volume of the simulated voxel was  $39\times39\times32~\mu\text{m}^3$ .

#### 3.3.2. Simulation details

Three simulation experiments were performed. Simulation 1 was performed using QTE and simulations 2 and 3 using TDE. The TDE waveforms encoding spherical b-tensors consist of three gradient pulse pairs with orthogonal directions and with identical diffusion encoding times  $(\delta)$ , diffusion times  $(\Delta)$ , and gradient magnitudes. Similarly to DDE, the

difference between the onset of the subsequent gradient pulses with orthogonal directions is referred to as mixing time ( $\tau$ ).

In each simulation,  $3\cdot 10^6$  random walks were generated using diffusivity of 2  $\mu m^2/ms$ .  $5\cdot 10^3$  random walkers were randomly placed inside each fibre and  $1.095\cdot 10^6$  in the extra-axonal space. Step length l was 0.31  $\mu m$  and duration dt was 8.1  $\mu s$ . When a random walker collided with a surface, it was elastically reflected off the collision point in such a way that the walkers total path length during dt was equal to l.

#### 3.3.3. Simulation 1

Simulation 1 was performed using the same waveforms as the imaging experiments (Fig. 1A-B).  $10^4$  time steps were used.

#### 3.3.4. Simulation 2

Following the approach proposed by Lundell et al. (2019, 2017), Simulation 2 was performed with the waveforms shown in Figs. 1A and 1 C ( $\delta$  = 35 ms,  $\Delta$  =  $\tau$  = 44 ms) to reduce the parameter bias due to spectral anisotropy of the spherical waveform and the discrepancy between the diffusion times of the waveforms encoding linear and spherical btensors. The power spectra of the Cartesian components of the unrotated TDE waveform (Fig. 1G) matches that of the linear waveform (Fig. 1E). It is important to note that the power spectrum of the unrotated TDE waveform is identical along x, y, and z but not along arbitrary directions. 31,720 time steps were used to keep the step length consistent with Simulation 1.

#### 3.3.5. Simulation 3

To further reduce the effects of time-dependent diffusion, Simulation 3 was performed with TDE waveforms with short pulses, and long diffusion and mixing times ( $\delta=3$  ms,  $\Delta=\tau=100$  ms). The long mixing time allows the random walkers to more fully sample their environments, minimizing the correlations between their positions during the different gradient pulse pairs. This is an important requirement for  $\mu FA$  estimation with DDE and TDE, which does not require the assumption of time-independent Gaussian intra-compartmental diffusion (Jespersen et al., 2013; 2019). The waveform encoding spherical b-tensors is shown in Fig. 1D. The waveform encoding linear b-tensors was a TDE waveform with the same direction for the three pulse pairs and with the same pulse length, diffusion time, and mixing time as the spherical waveform. 62,195 time steps were used to keep the step length consistent with Simulation 1.

## 3.3.6. Noise addition

To study the precision of  $\mu FA$ , SNR of the simulated signals was lowered to 25. Signals with Rician noise (Gudbjartsson and Patz, 1995) were generated as

$$S_{\text{noisy}} = \sqrt{(S+X)^2 + Y^2},$$
 (20)

where S is the simulated signal without noise and X and Y are randomly sampled from a normal distribution with zero mean and standard deviation  $\sigma$ . Here, SNR refers to the signal without diffusion-weighting divided by  $\sigma$ . Noise addition was performed  $10^4$  times.

To confirm that the noise due to finite number of spins was much less than the added noise, Simulation 1 was repeated 5 times with different pseudorandom number generator seeds. SNR, estimated as the signal without diffusion-weighting divided by the mean standard deviation of the signals generated with different seeds, was 5,027.

# 3.3.7. Ground-truth μFA

The ground-truth  $\mu FA$  was calculated according to Eq. (2) by separately fitting diffusion tensors to the LTE signals from each compartment, i.e., the individual fibres and extra-axonal space. The diffusion tensors were estimated by fitting diffusion and kurtosis tensors (Jensen et al., 2005) to data using a weighted linear least squares algorithm in Dipy (Garyfallidis et al., 2014). To vary the ground-truth  $\mu FA$ , three signal fractions for the spins in the intra-axonal space ( $f_{intra}$ ) were

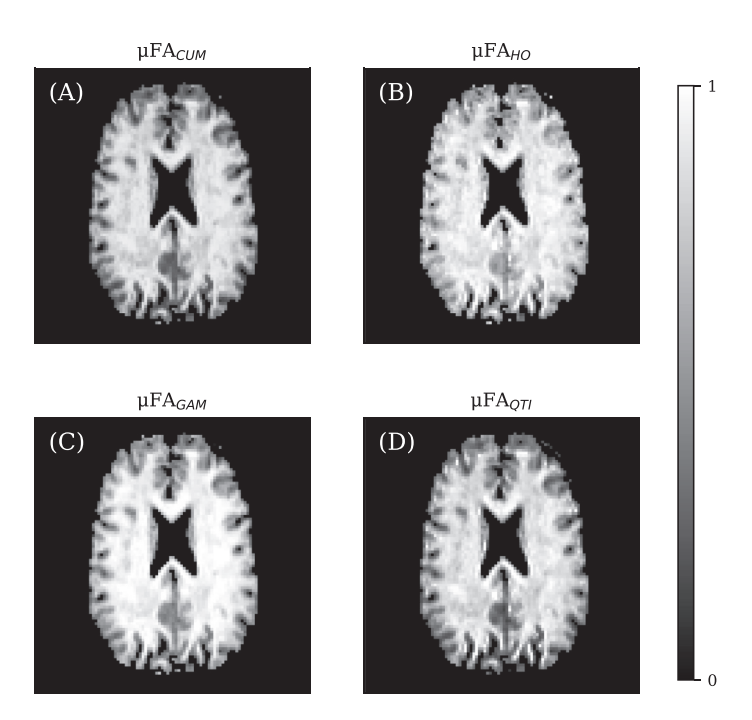


Fig. 4. Representative axial slices of the  $\mu$ FA maps in one of the volunteers calculated using the cumulant model (A), higher-order model (B), gamma model (C), and OTI (D).

used: 0.2, 0.6, and 1. The total signal was calculated as a weighted sum of the signals from the walkers in the intra- and extra-axonal spaces.

#### 4. Results

# 4.1. Imaging experiments

# 4.1.1. Volunteer experiments

Representative axial slices of the  $\mu FA$  maps in one of the volunteers are shown in Fig. 4. A visual inspection reveals that the higher-order model and gamma model result in greater  $\mu FA$  values than the cumulant model and QTI. The best agreement, as measured by the concordance correlation coefficient, was found between the cumulant model and QTI ( $\rho_c=0.91$ ), followed by the cumulant model and gamma model ( $\rho_c=0.85$ ), higher-order model and gamma model ( $\rho_c=0.85$ ), gamma model and QTI ( $\rho_c=0.81$ ), higher-order model and QTI ( $\rho_c=0.64$ ), and cumulant model and higher-order model ( $\rho_c=0.64$ ).

Fig. 5 shows representative axial slices of the difference maps in one of the volunteers. The cumulant model and QTI produced very similar maps.  $\mu FA$  maps estimated using the higher-order model exhibited smaller contrast between gray matter and white matter than the other methods, as can be seen particularly clearly in Fig. 5D. The gamma model produced greater values of  $\mu FA$  than the cumulant model and QTI consistently across the brain. In white matter, the gamma model also produced greater values of  $\mu FA$  than the higher-order model.

The Bland-Altman plots in Fig. 6 show the voxel-wise differences between the methods'  $\mu$ FA estimates against their mean values across all volunteers. The good agreement between the cumulant model and QTI can be seen in the small mean difference (0.02) and the relatively small width of the 95% central range of the differences (0.18). Because  $P_3$  was constrained to be negative, the higher-order model resulted in higher values of  $\mu$ FA than the cumulant model in each voxel. On average, the higher-order model produced greater values of  $\mu$ FA than the other methods, especially at lower values of  $\mu$ FA, which are found in gray matter. When averaged over the whole brain,  $\mu$ FA values produced by the gamma model were 0.12 greater than the cumulant model and 0.10 greater than QTI.

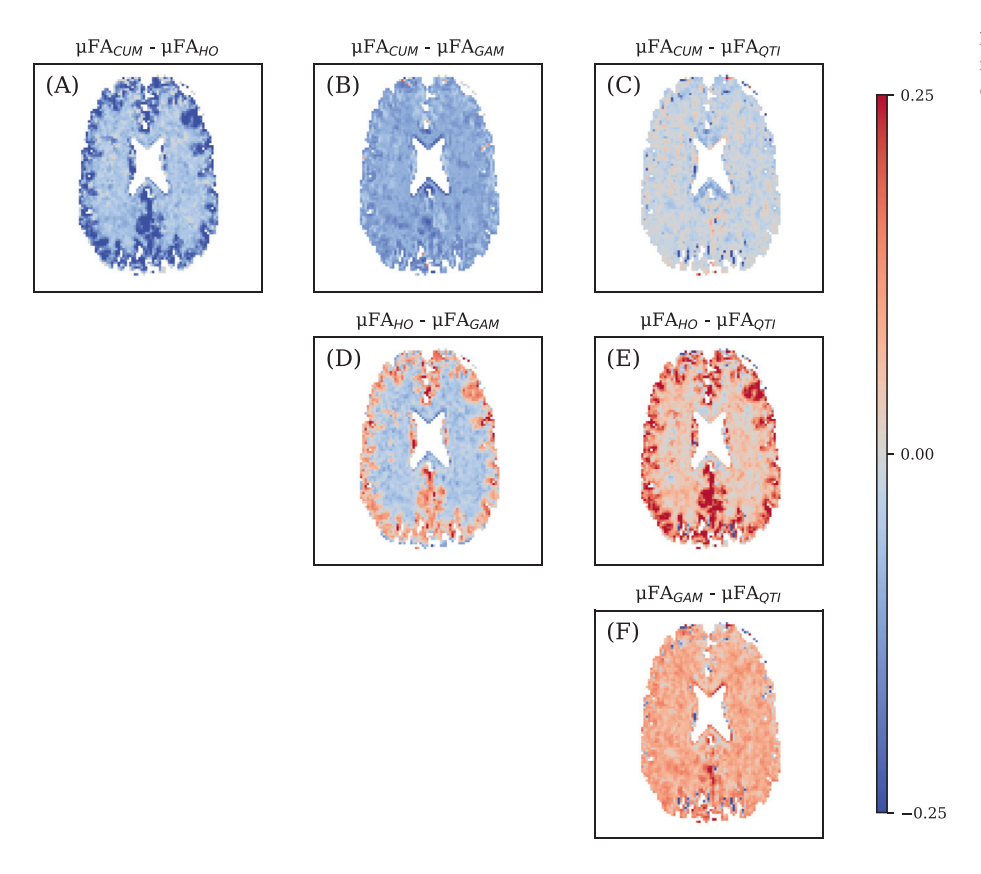


**Fig. 5.** Representative axial slices of the difference maps highlighting the differences between the methods' µFA estimates in one of the volunteers.

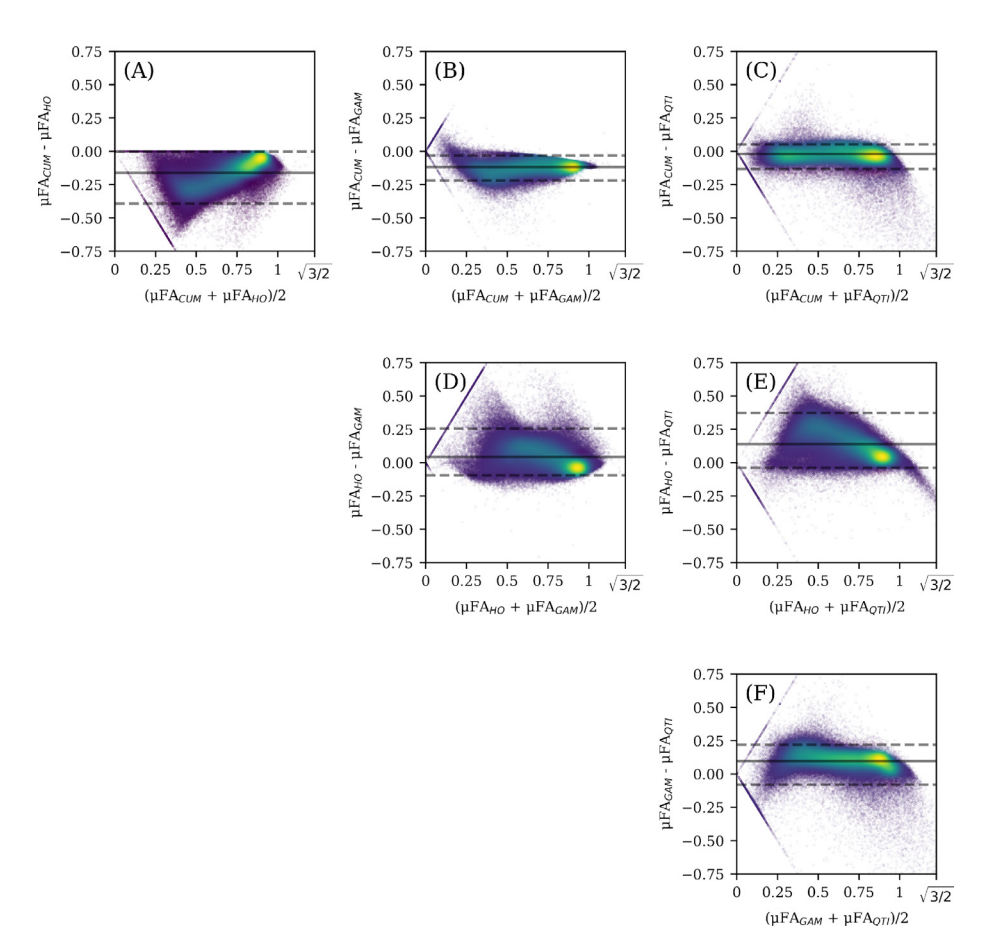


Fig. 6. Voxel-wise comparison of the  $\mu$ FA maps. The differences are plotted against their mean value. The solid lines depict the mean difference. The dashed lines show the 2.5th and the 97.5th percentiles of the distribution of the differences. Colour represents data point density.

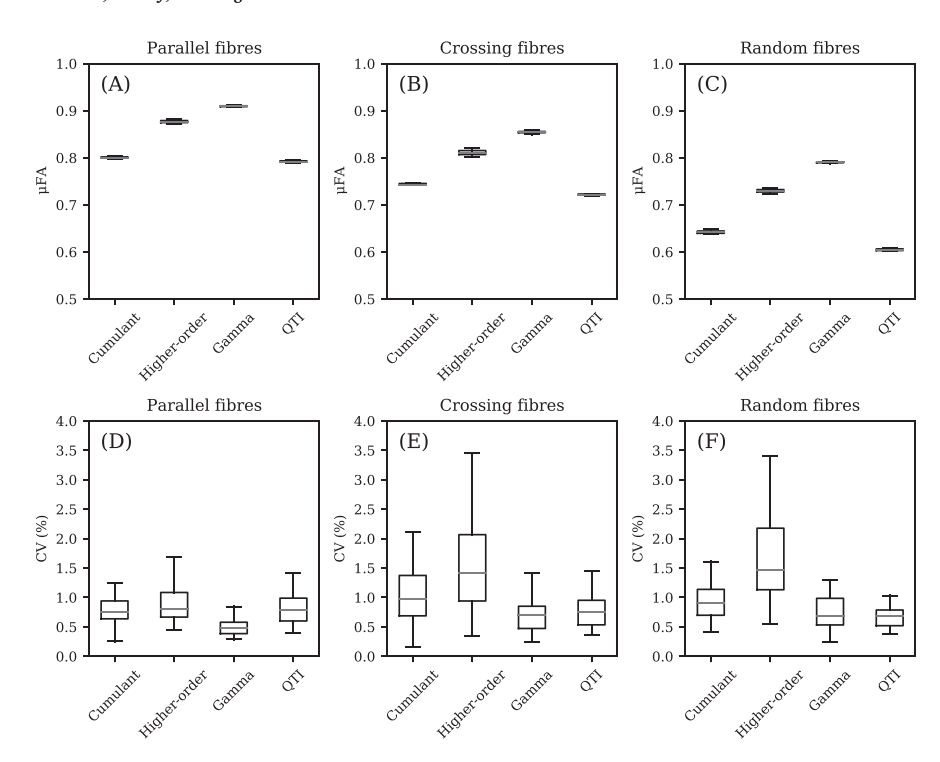


Fig. 7. The results of the phantom experiments. (A-C)  $\mu$ FA values averaged over the phantom ROIs from the repeated acquisitions. (D-F) The distributions of the voxel-level coefficients of variation. The blue line denotes the median. The box spans the interquartile range. The whiskers extend to the furthest data point within 1.5  $\cdot$  IQR from the 1st or the 3rd quartile.

A significant correlation ( $R^2=0.13, p<10^{-3}$ ) was found between the FA maps (provided in the supplementary information) calculated from the data acquired with linear and spherical b-tensors, revealing that the acquisition with isotropic diffusion-weighting was moderately orientationally variant.

The average SNR, as quantified by the mean signal divided by the standard deviation over the images without diffusion-weighting, was 28.

## 4.1.2. Phantom experiments

 $\mu FA$  values averaged over the phantom ROIs from the repeated acquisitions are shown in Fig. 7A-C. The gamma model consistently resulted in the greatest values of  $\mu FA$ , followed by the higher-order model, cumulant model, and QTI. The differences in mean  $\mu FA$  calculated using the different signal models were statistically significant in all pair-wise comparisons using an independent samples t-test ( $p < 10^{-3}$ ). Despite the smaller fibre radius,  $\mu FA$  was the lowest in the ROI with randomly oriented fibres due to the lower packing density of the microfibres.

The distributions of the voxel-level CVs are shown in Fig. 7D-F. The median CVs were well below 2%, indicating good repeatability in voxels with high  $\mu$ FA. The higher-order model stood out for having the lowest repeatability, especially in the phantom ROIs with crossing or randomly oriented fibres. A significant correlation ( $R^2 = 0.11$ ,  $p < 10^{-3}$ ) was found between the FA maps calculated from the data acquired with waveforms encoding linear and spherical b-tensors.

The average SNR was 123 as quantified by the mean signal divided by the standard deviation over the images without diffusion-weighting.

## 4.2. Simulation experiments

The results of the simulation experiments are presented in Fig. 8. The ground-truth  $\mu$ FA was 0.34 for  $f_{\rm intra}=0.2$ , 0.59 for  $f_{\rm intra}=0.6$ , and 0.97 for  $f_{\rm intra}=1$ . Furthermore, Bland-Altman plots of the simulation results are presented in Fig. 9.

In Simulation 1, all methods overestimated  $\mu FA$  and the bias was greater at lower values of ground-truth  $\mu FA$  (Fig. 8A-C). In Simulation 2, the application of the TDE waveform whose power spectrum along three orthogonal directions matches that of the linear waveform reduced the overestimation of  $\mu FA$  for all methods (Fig. 8D-F). In Simulation 3,

the application of the TDE waveforms with short pulses, long diffusion times, and long mixing times further reduced the bias (Fig. 8G-I). These results show that both the discrepancy between the diffusion times of the waveforms encoding different b-tensor shapes, and the correlations between the spins' positions during the diffusion encoding along different directions can result in overestimation of  $\mu$ FA. However, the simulations suggest that the bias is small in white matter, where  $\mu$ FA is high. The average positive bias caused by time-dependent diffusion, i.e., the difference between the expected  $\mu$ FA in simulations 1 and 3, was 0.11 for  $f_{intra} = 0.2$ , 0.09 for  $f_{intra} = 0.6$ , and 0.04 for  $f_{intra} = 1$ .

The accuracy of the signal models for  $\mu FA$  estimation was assessed using the results from Simulation 3 which are not confounded by the bias induced by time-dependent diffusion. The mean squared error (MSE) between the expected value of  $\mu FA$  and the ground-truth value was  $1.8 \cdot 10^{-3}$  for the cumulant model,  $5.4 \cdot 10^{-3}$  for the higher-order model,  $12.7 \cdot 10^{-3}$  for the gamma model and  $1.6 \cdot 10^{-3}$  for QTI. In terms of precision, the average CV of  $\mu FA$  was 6.6% for the cumulant model, 10.6% for the higher-order model, 6.6% for the gamma model, and 8.5% for QTI. However,  $\mu FA$  is heteroscedastic and the precision of each method strongly depended on the ground-truth  $\mu FA$ .

The higher-order model is motivated by the b-value-dependent underestimation of  $\mu FA$  using the cumulant model. Indeed, the higher-order model produced more accurate estimates of  $\mu FA$  when the cumulant model underestimated  $\mu FA$ . However, because  $\textit{P}_3$  was constrained to be non-negative, the higher-order model could not produce lower values of  $\mu FA$  and thus it provided even more inaccurate estimates in situations where the cumulant model overestimated  $\mu FA$ . Allowing  $\textit{P}_3$  to take negative values improved the accuracy (MSE = 2.0  $\cdot$  10 $^{-3}$ .) but greatly destabilized the fit (mean CV = 24%). In most cases, at the b-values used in the simulations, the underestimation due to the invalidity of the cumulant expansion of the powder-averaged signal was not strong enough to cancel the overestimation.

## 5. Discussion

Over recent years, MDE methods have gained significant attention for their ability to disentangle the orientation dispersion of anisotropic microscopic diffusion environments and the size variance of microscopic

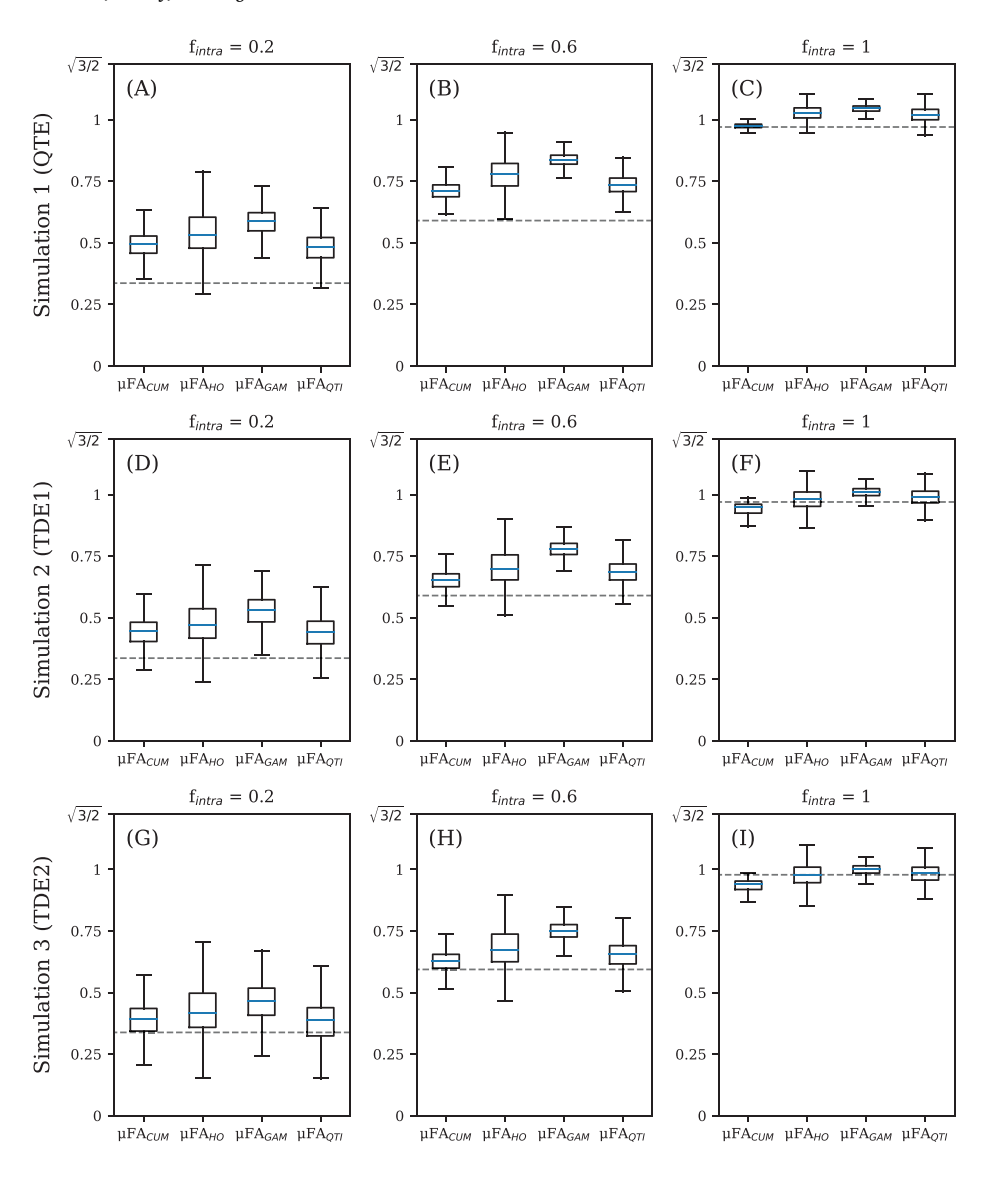


**Fig. 8.** The distributions of the μFA estimates calculated from the simulated signals after  $10^4$  repetitions of noise addition to lower SNR to 25.  $f_{imtra}$  is the signal fraction of the intra-axonal space. (A-C) Results of Simulation 1. (D-F) Results of Simulation 2. (G-I) Results of Simulation 3. The dashed line denotes the ground-truth μFA. The blue line denotes the median. The box spans the interquartile range. The whiskers extend to the furthest data point within  $1.5 \cdot \text{IQR}$  from the 1st or the 3rd quartile

diffusion environments, enabling microscopic diffusion anisotropy to be measured without a priori information about tissue microstructure. Several microscopic diffusion anisotropy estimation methods have been introduced (de Almeida Martins and Topgaard, 2016; Henriques et al., 2020a; Ianuş et al., 2018; Jespersen et al., 2013; Lasič et al., 2014; Westin et al., 2016), yet the differences between the methods have received little attention thus far. The purpose of this study was to assess the accuracy and precision of µFA estimates calculated using different signal models. µFA was chosen as the metric of interest for its connection to conventional FA that is well known in the neuroscience community. The cumulant model, gamma model, and QTI were chosen as the signal models of interest for their numerous applications in recent neuroimaging studies (Andersen et al., 2020; Kamiya et al., 2020; Lampinen et al., 2020; Szczepankiewicz et al., 2015; 2016; Westin et al., 2016; Yang et al., 2018). The higher-order model was included in the study for it being a simple extension to the cumulant model that has been shown to improve the accuracy of µFA estimation in animal studies using DDE (Ianus et al., 2018). To our knowledge, only two studies have previously focused on comparing µFA estimation methods: Ianus et al. (2015) compared the cumulant model using DDE to the gamma model using TDE, and Reymbaut et al. (2020) compared the gamma model, QTI, and Monte Carlo inversion methods by explicitly modelling the tissue as a distribution of microscopic diffusion tensors using Eq. (1).

In another relevant study, Martin et al. (2020) estimated the covariance tensor using QTI and investigated how  $\mu$ FA relates to other microscopic diffusion anisotropy indices in terms of contrast-to-noise ratio. In this study, four  $\mu$ FA estimation methods were applied on MRI data acquired using a clinical whole-body scanner and on synthetic data generated by simulating time-dependent diffusion.

In this study, the gamma model suffered from the greatest bias in the simulation experiments and consistently produced greater µFA values than the other methods in healthy white matter, fibre phantom, and simulations. The disagreement between the gamma model and the other methods was expected as the gamma model assumes the distribution of apparent microscopic diffusivities to follow a gamma distribution whereas the other methods are based on the truncated cumulant expansion. It is important to emphasize that although the assumption of gamma-distributed axon radii may be justified in real tissues (Lee et al., 2019), the radii of our simulated axons did not follow a gamma distribution (Fig. 3B). Furthermore, gamma-distributed axon radii is not a sufficient condition for the apparent diffusivities to follow a gamma distribution. Reymbaut et al. (2020) have also reported that the gamma model produces biased estimates when the signal strongly deviates from a monoexponential decay, as is the case in white matter. However, they also reported that QTI results in biased estimates in the case of significant size variance of microsocpic diffusion environments. Therefore,

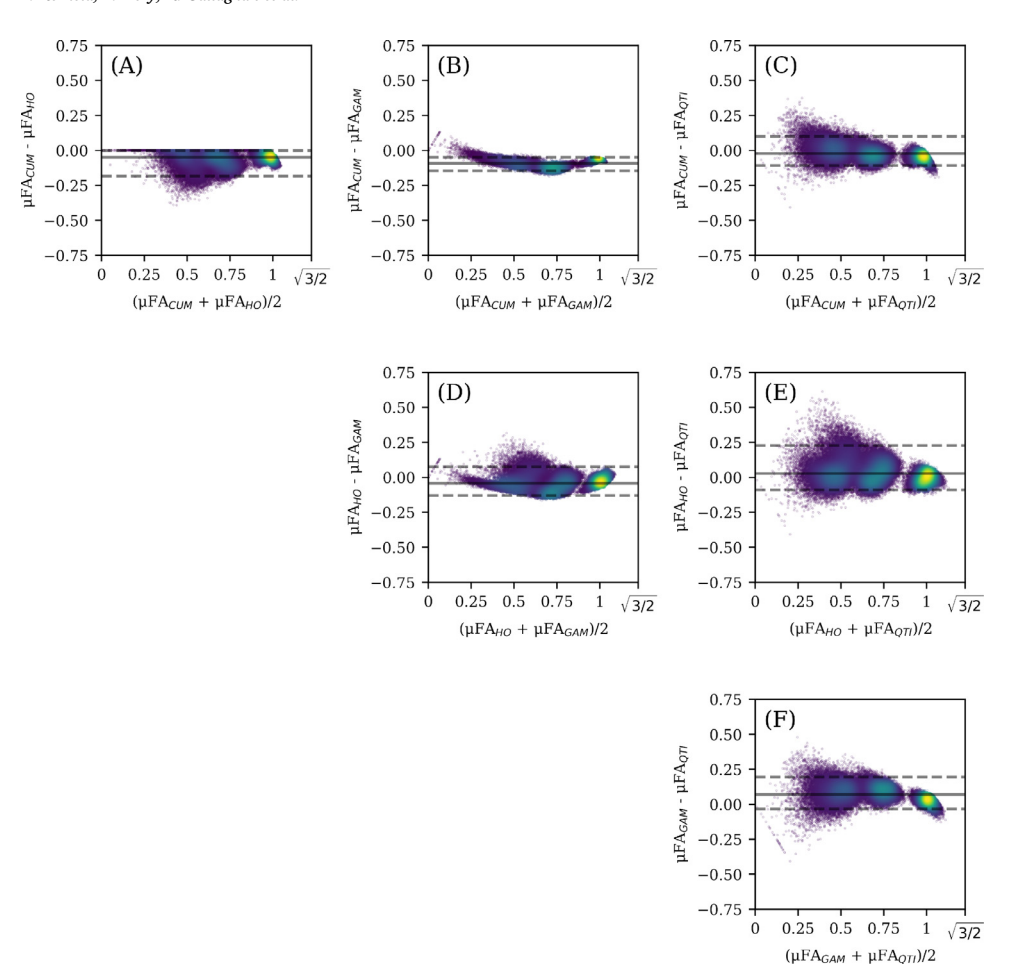


Fig. 9. Comparison of the  $\mu$ FA estimates calculated from the simulated data. The differences are plotted against their mean value. The solid lines depict the mean difference. The dashed lines show the 2.5th and the 97.5th percentiles of the distribution of the differences. Colour represents data point density.

given the microstructure-dependent bias, the results presented here can not be generalized to all situations. Nevertheless, our results showed a consistent disagreement between the gamma model and the second order cumulant expansion, which must be taken into account when interpreting reported results.

In terms of precision, the higher-order model stood out for being the most sensitive to noise. This is most likely explained by the third order polynomial fit's sensitivity to signal variation. Allowing  $P_3$  to take negative values further destabilized the fit. The higher-order model's low precision probably prevents it from being useful in most human neuroimaging studies. In the phantom experiments, the voxel-specific CV of  $\mu$ FA from all methods was low with the majority CV values being well below 2%, indicating very good repeatability in voxels with high microscopic diffusion anisotropy. However, since the phantom contained highly anisotropic microfibres, this result was expected based on previous reports of how the precision of  $\mu$ FA is high in voxels with high  $\mu$ FA but quickly diminishes with a decreasing value of  $\mu$ FA (Ianuş et al., 2016; Kerkelä et al., 2020; Lasič et al., 2014; Szczepankiewicz et al., 2015; 2019b).

The  $\mu FA$  estimation methods used here assume intra-compartmental kurtosis to be negligible, which can result in biased estimates in the case of time-dependent diffusion (Henriques et al., 2020a; 2021). Our simulation experiments showed that the combination of trapezoidal linear gradient waveforms and isotropic encoding with QTE can lead to a significant overestimation of  $\mu FA$ , a result that has been discussed in detail by Lundell et al. (2019). As a solution, they proposed designing the linear waveform so that its power spectrum matches that of the spherical waveform at least along one direction. Indeed, in the simulations, the accuracy of  $\mu FA$  estimates was improved when the power spectra were matched. However, the simulations also showed that this is not

sufficient for accurate estimation of  $\mu FA$ . The accuracy of  $\mu FA$  further improved when a TDE waveform with short pulses, long diffusion time, and long mixing time was applied, eliminating the correlations between the positions of the random walkers during the applications of the gradient pulse pairs, an important assumption in the theory of  $\mu FA$  estimation with DDE (Jespersen et al., 2013). However, the simulated TDE waveforms are completely unrealistic in today's human neuroimaging experiments because of their duration and gradient strength requirements. Considering that the bias in  $\mu FA$  induced by time-dependent diffusion was small when the ground-truth  $\mu FA$  was high, as is the case in white matter, and the effects of time-dependent diffusion are easier to observe in Monte Carlo random walk simulations than in the brain (Gyori et al., 2020), these results support using QTE for  $\mu FA$  estimation in human white matter.

This study has several limitations. Most importantly, the accuracy and precision of µFA estimation depend on the details of the acquisition protocol which was kept constant here. For instance, the effect of b-values and diffusion encoding directions was outside the scope of this study. Also, the problem of designing optimal gradient waveforms for MDE experiments, discussed in detail by Szczepankiewicz et al. (2020), was outside the scope of this study. Furthermore, our acquisitions with the lowest b-value may be affected by perfusion effects that may cause parameter bias. However, the focus of this study was to assess the performance of the signal models relative to each other when applied on the same data. It also must be mentioned that the microfibre phantom used for studying the precision of  $\mu FA$  contains fibres that are too large to be representative of white matter microstructure. In the simulations, the effects of orientation dispersion, distribution of axon radii, packing density, and membrane permeability were not assessed because the simulated geometry was kept constant across the simulations. Also, the periodic boundary conditions introduced unrealistic periodicity into the simulated microstructure. Nevertheless, the simulated fibre geometry, generated using the algorithm by Callaghan et al. (2020), resembles real axons and enabled the  $\mu$ FA estimates to be compared to a known ground truth. Finally, although Lee et al. (2021, 2020) have shown that a larger number of random walkers may be necessary to accurately calculate the moments of the displacement distribution, we only analyzed the simulated signal, which had converged, as shown by our results that are in good agreement with previously reported results (Callaghan et al., 2020; Hall and Alexander, 2009; Rafael-Patino et al., 2020). Future studies should address the mentioned limitations to facilitate the optimal use of  $\mu$ FA.

#### 6. Conclusion

The gamma-distributed diffusivities assumption produced greater values of  $\mu FA$  than the second order cumulant expansion. The simulations showed that matching the power spectrum of the linear waveform to the power spectrum of a component of the spherical waveform is not sufficient for accurate estimation of  $\mu FA$ . Nevertheless, the simulations suggest that the bias in  $\mu FA$  caused by time-dependent diffusion is small in human white matter.

## Data and code availability

Code for reproducing the results will be made available at https://github.com/kerkelae/ufa-model-comparison.

## **Declaration of Competing Interest**

FS is an inventor on a patent related to the study.

# Credit authorship contribution statement

Leevi Kerkelä: Conceptualization, Data curation, Formal analysis, Investigation, Methodology, Project administration, Software, Validation, Visualization, Writing – original draft. Fabio Nery: Conceptualization, Investigation, Writing – review & editing. Ross Callaghan: Resources, Writing – review & editing. Resources, Writing – review & editing. Noemi G. Gyori: Conceptualization, Validation, Writing – review & editing. Filip Szczepankiewicz: Resources, Writing – review & editing. Marco Palombo: Resources, Writing – review & editing. Geoff J.M. Parker: Resources, Writing – review & editing. Hui Zhang: Resources, Writing – review & editing. Matt G. Hall: Resources, Supervision, Writing – review & editing. Chris A. Clark: Funding acquisition, Resources, Supervision, Writing – review & editing.

## Acknowledgements

LK was supported by the NIHR GOSH BRC. FN was supported by GOSH Children's Charity (V0318). FLZ was supported by NIHR UCLH Biomedical Research Centre (BRC) grant, and UK-MRC ImagingBioPro grant (MR/R025673/1), and UCL Department of Medical Physics and Biomedical Engineering and EPSRC (EP/M020533/1; CMIC Pump-Priming Award). NGG was funded by UK BBSRC820 BB/M009513/1. MP was supported by UKRI Future Leaders Fellowship (MR/T020296/1).

#### Supplementary material

Supplementary material associated with this article can be found, in the online version, at 10.1016/j.neuroimage.2021.118445

#### References

- de Almeida Martins, J.P., Topgaard, D., 2016. Two-dimensional correlation of isotropic and directional diffusion using nmr. Phys. Rev. Lett. 116 (8), 087601.
- Andersen, K.W., Lasič, S., Lundell, H., Nilsson, M., Topgaard, D., Sellebjerg, F., Szczepankiewicz, F., Siebner, H.R., Blinkenberg, M., Dyrby, T.B., 2020. Disentangling white-matter damage from physiological fiber orientation dispersion in multiple sclerosis. Brain Commun.
- Andersson, J.L., Sotiropoulos, S.N., 2016. An integrated approach to correction for off-resonance effects and subject movement in diffusion mr imaging. Neuroimage 125, 1063–1078.
- Assaf, Y., Johansen-Berg, H., Thiebaut de Schotten, M., 2019. The role of diffusion mri in neuroscience. NMR Biomed. 32 (4), e3762.
- Basser, P.J., Mattiello, J., LeBihan, D., 1994. Mr diffusion tensor spectroscopy and imaging. Biophys. J. 66 (1), 259–267.
- Branch, M.A., Coleman, T.F., Li, Y., 1999. A subspace, interior, and conjugate gradient method for large-scale bound-constrained minimization problems. SIAM J. Sci. Comput. 21 (1), 1–23.
- Callaghan, R., Alexander, D.C., Palombo, M., Zhang, H., 2020. Config: contextual fibre growth to generate realistic axonal packing for diffusion MRI simulation. Neuroimage 220, 117107.
- Clark, C.A., Hedehus, M., Moseley, M.E., 2002. In vivo mapping of the fast and slow diffusion tensors in human brain. Magn. Reson. Med. 47 (4), 623–628.
- Cory, D., Garroway, A., Miller, J., 1990. Applications of spin transport as a probe of local geometry. In: Abstracts of Papers of the American Chemical Society, 199. Amer ChemicalSoc 1155 16th St, NW, Washington, DC 20036, pp. 105–POLY.
- Eriksson, S., Lasic, S., Topgaard, D., 2013. Isotropic diffusion weighting in pgse nmr by magic-angle spinning of the q-vector. J. Magn. Reson. 226, 13–18.
- Garyfallidis, E., Brett, M., Amirbekian, B., Rokem, A., Van Der Walt, S., Descoteaux, M., Nimmo-Smith, I., 2014. Dipy, a library for the analysis of diffusion mri data. Front Neuroinform 8, 8.
- Gudbjartsson, H., Patz, S., 1995. The rician distribution of noisy mri data. Magn. Reson. Med. 34 (6), 910–914.
- Gyori, N., Hall, M.G., Clark, C.A., Alexander, D.C., Kaden, E., 2020. Discrepancy between in-vivo measurements and monte-carlo simulations with spherical structures in b-tensor encoding. In: International Society for Magnetic Resonance in Medicine and Society for MR Radiographers & Technologists Virtual Conference & Exhibition.
- Hall, M.G., Alexander, D.C., 2009. Convergence and parameter choice for monte-carlo simulations of diffusion mri. IEEE Trans. Med. Imaging 28 (9), 1354–1364.
- Henriques, R.N., Jespersen, S.N., Shemesh, N., 2019. Microscopic anisotropy misestimation in spherical-mean single diffusion encoding mri. Magn. Reson. Med. 81 (5), 3245–3261.
- Henriques, R.N., Jespersen, S.N., Shemesh, N., 2020. Correlation tensor magnetic resonance imaging. Neuroimage 211, 116605.
- Henriques, R.N., Jespersen, S.N., Shemesh, N., 2021. Evidence for microscopic kurtosis in neural tissue revealed by correlation tensor mri. arXiv preprint arXiv:2102.11701.
- Henriques, R.N., Palombo, M., Jespersen, S.N., Shemesh, N., Lundell, H., Ianus, A., 2020. Double diffusion encoding and applications for biomedical imaging. J. Neurosci. Methods 108989.
- Ianuş, A., Drobnjak, I., Alexander, D.C., 2016. Model-based estimation of microscopic anisotropy using diffusion MRI: a simulation study. NMR Biomed. 29 (5), 672–685.
- Ianuş, A., Drobnjak, I., Shemesh, N., Alexander, D., 2015. Metrics of microscopic anisotropy: a comparison study. In: International Conference on Magnetic Resonance Microscopy.
- Ianuş, A., Jespersen, S.N., Duarte, T.S., Alexander, D.C., Drobnjak, I., Shemesh, N., 2018.
  Accurate estimation of microscopic diffusion anisotropy and its time dependence in the mouse brain. Neuroimage 183, 934–949.
- Jelescu, I.O., Budde, M.D., 2017. Design and validation of diffusion MRI models of white matter. Front. Phys. 5, 61.
- Jenkinson, M., Beckmann, C.F., Behrens, T.E., Woolrich, M.W., Smith, S.M., 2012. Fsl. Neuroimage 62 (2), 782–790.
- Jensen, J.H., Helpern, J.A., 2010. Mri quantification of non-gaussian water diffusion by kurtosis analysis. NMR Biomed. 23 (7), 698–710.
- Jensen, J.H., Helpern, J.A., Ramani, A., Lu, H., Kaczynski, K., 2005. Diffusional kurtosis imaging: the quantification of non-gaussian water diffusion by means of magnetic resonance imaging. Magn. Reson. Med 53 (6), 1432–1440.
- Jespersen, S.N., Kroenke, C.D., Østergaard, L., Ackerman, J.J., Yablonskiy, D.A., 2007. Modeling dendrite density from magnetic resonance diffusion measurements. Neuroimage 34 (4), 1473–1486.
- Jespersen, S.N., Lundell, H., Sønderby, C.K., Dyrby, T.B., 2013. Orientationally invariant metrics of apparent compartment eccentricity from double pulsed field gradient diffusion experiments. NMR Biomed. 26 (12), 1647–1662.
- Jespersen, S.N., Olesen, J.L., Ianuş, A., Shemesh, N., 2019. Effects of nongaussian diffusion on \(\tilde{e}\)isotropic diffusiong measurements: an ex-vivo microimaging and simulation study. J. Magn. Reson. 300, 84–94.
- Johansen-Berg, H., Behrens, T.E., 2013. Diffusion MRI: From Quantitative Measurement to in vivo Neuroanatomy. Academic Press.
- Jones, D.K., Cercignani, M., 2010. Twenty-five pitfalls in the analysis of diffusion mri data. NMR Biomed. 23 (7), 803–820.
- Kamiya, K., Kamagata, K., Ogaki, K., Hatano, T., Ogawa, T., Takeshige-Amano, H., Murata, S., Andica, C., Murata, K., Feiweier, T., et al., 2020. Brain white-matter degeneration due to aging and parkinson disease as revealed by double diffusion encoding. Front. Neurosci. 14, 1091.
- Kellner, E., Dhital, B., Kiselev, V.G., Reisert, M., 2016. Gibbs-ringing artifact removal based on local subvoxel-shifts. Magn. Reson. Med. 76 (5), 1574–1581.

- Kerkelä, L., Henriques, R.N., Hall, M.G., Clark, C.A., Shemesh, N., 2020. Validation and noise robustness assessment of microscopic anisotropy estimation with clinically feasible double diffusion encoding mri. Magn. Reson. Med. 83 (5), 1698–1710.
- Kerkelä, L., Nery, F., Hall, M.G., Clark, C.A., 2020. Disimpy: a massively parallel monte carlo simulator for generating diffusion-weighted mri data in python. J. Open Sour. Softw. 5 (52), 2527.
- Koch, M.A., Finsterbusch, J., 2008. Compartment size estimation with double wave vector diffusion-weighted imaging. Magn. Reson. Med 60 (1), 90–101.
- Lampinen, B., Szczepankiewicz, F., Mårtensson, J., van Westen, D., Sundgren, P.C., Nilsson, M., 2017. Neurite density imaging versus imaging of microscopic anisotropy in diffusion mri: a model comparison using spherical tensor encoding. Neuroimage 147, 517-531.
- Lampinen, B., Zampeli, A., Björkman-Burtscher, I.M., Szczepankiewicz, F., Källén, K., Compagno Strandberg, M., Nilsson, M., 2020. Tensor-valued diffusion mri differentiates cortex and white matter in malformations of cortical development associated with epilepsy. Epilepsia 61 (8), 1701–1713.
- Lasič, S., Szczepankiewicz, F., Eriksson, S., Nilsson, M., Topgaard, D., 2014. Microanisotropy imaging: quantification of microscopic diffusion anisotropy and orientational order parameter by diffusion MRI with magic-angle spinning of the q-vector. Front. Phys. 2, 11.
- Lee, H.-H., Fieremans, E., Novikov, D.S., 2021. Realistic microstructure simulator (RMS): monte carlo simulations of diffusion in three-dimensional cell segmentations of microscopy images. J. Neurosci. Methods 350, 109018.
- Lee, H.-H., Jespersen, S.N., Fieremans, E., Novikov, D.S., 2020. The impact of realistic axonal shape on axon diameter estimation using diffusion mri. Neuroimage 223, 117228
- Lee, H.-H., Yaros, K., Veraart, J., Pathan, J.L., Liang, F.-X., Kim, S.G., Novikov, D.S., Fieremans, E., 2019. Along-axon diameter variation and axonal orientation dispersion revealed with 3d electron microscopy: implications for quantifying brain white matter microstructure with histology and diffusion mri. Brain Struct. Funct. 224 (4), 1469–1488
- Lin, L., 1989. A concordance correlation coefficient to evaluate reproducibility. Biometrics 255–268.
- Lundell, H., Nilsson, M., Dyrby, T., Parker, G., Cristinacce, P.H., Zhou, F.-L., Topgaard, D., Lasič, S., 2019. Multidimensional diffusion MRI with spectrally modulated gradients reveals unprecedented microstructural detail. Sci. Rep. 9 (1), 1–12.
- Lundell, H.M.H., Nilsson, M., Dyrby, T.B., Parker, G.J., Cristinacce, P.L.H., Zhou, F.-l., Topgaard, D., Lasic, S., 2017. Microscopic anisotropy with spectrally modulated q-space trajectory encoding. International Society for Magnetic Resonance in Medicine 2017
- Mardia, K.V., Jupp, P.E., 2009. Directional Statistics, 494. John Wiley & Sons.
- Martin, J., Endt, S., Wetscherek, A., Kuder, T.A., Doerfler, A., Uder, M., Hensel, B., Laun, F.B., 2020. Contrast-to-noise ratio analysis of microscopic diffusion anisotropy indices in q-space trajectory imaging. Zeitschrift für Medizinische Physik 30 (1), 4–16.
- Mitra, P.P., 1995. Multiple wave-vector extensions of the NMRpulsed-field-gradient spin-echo diffusion measurement. Phys. Rev. B 51 (21), 15074.
- Nery, F., Szczepankiewicz, F., Kerkelä, L., Hall, M.G., Kaden, E., Gordon, I., Thomas, D.L., Clark, C.A., 2019. In vivo demonstration of microscopic anisotropy in the human kidney using multidimensional diffusion MRI. Magn. Reson. Med. 82 (6), 2160–2168.
- Novikov, D.S., Fieremans, E., Jespersen, S.N., Kiselev, V.G., 2019. Quantifying brain microstructure with diffusion MRI: theory and parameter estimation. NMR Biomed. 32 (4), e3998.
- Novikov, D.S., Kiselev, V.G., 2010. Effective medium theory of a diffusion-weighted signal. NMR Biomed. 23 (7), 682–697.
- Palombo, M., Alexander, D.C., Zhang, H., 2019. A generative model of realistic brain cells with application to numerical simulation of the diffusion-weighted mr signal. Neuroimage 188, 391–402.
- Rafael-Patino, J., Romascano, D., Ramirez-Manzanares, A., Canales-Rodríguez, E.J., Girard, G., Thiran, J.-P., 2020. Robust monte-carlo simulations in diffusion-mri: effect of the substrate complexity and parameter choice on the reproducibility of results. Front. Neuroinform. 14, 8.
- Reymbaut, A., Mezzani, P., de Almeida Martins, J.P., Topgaard, D., 2020. Accuracy and precision of statistical descriptors obtained from multidimensional diffusion signal inversion algorithms. NMR Biomed. e4267.
- Shemesh, N., Jespersen, S.N., Alexander, D.C., Cohen, Y., Drobnjak, I., Dyrby, T.B., Finster-busch, J., Koch, M.A., Kuder, T., Laun, F., et al., 2016. Conventions and nomenclature for double diffusion encoding nmr and mri. Magn. Reson. Med. 75 (1), 82–87.

- Sjölund, J., Szczepankiewicz, F., Nilsson, M., Topgaard, D., Westin, C.-F., Knutsson, H., 2015. Constrained optimization of gradient waveforms for generalized diffusion encoding. J. Magn. Reson. 261, 157–168.
- Sotiropoulos, S.N., Behrens, T.E., Jbabdi, S., 2012. Ball and rackets: inferring fiber fanning from diffusion-weighted mri. Neuroimage 60 (2), 1412–1425.
- Stepišnik, J., 1993. Time-dependent self-diffusion by nmr spin-echo. Physica B 183 (4), 343–350.
- Strang, G., Borre, K., 1997. Linear algebra, geodesy, and GPS. Siam.
- de Swiet, T.M., Mitra, P.P., 1996. Possible systematic errors in single-shot measurements of the trace of the diffusion tensor. J. Magn. Reson. Series B 111 (1), 15–22.
- Szczepankiewicz, F., Hoge, S., Westin, C.-F., 2019. Linear, planar and spherical tensor-valued diffusion MRI data by free waveform encoding in healthy brain, water, oil and liquid crystals. Data Brief 25, 104208.
- Szczepankiewicz, F., Lasič, S., van Westen, D., Sundgren, P.C., Englund, E., Westin, C.-F., Ståhlberg, F., Lätt, J., Topgaard, D., Nilsson, M., 2015. Quantification of microscopic diffusion anisotropy disentangles effects of orientation dispersion from microstructure: applications in healthy volunteers and in brain tumors. Neuroimage 104, 241–252.
- Szczepankiewicz, F., Sjölund, J., Ståhlberg, F., Lätt, J., Nilsson, M., 2019. Tensor-valued diffusion encoding for diffusional variance decomposition (divide): technical feasibility in clinical mri systems. PLoS ONE 14 (3).
- Szczepankiewicz, F., van Westen, D., Englund, E., Westin, C.-F., Ståhlberg, F., Lätt, J., Sundgren, P.C., Nilsson, M., 2016. The link between diffusion mri and tumor heterogeneity: mapping cell eccentricity and density by diffusional variance decomposition (divide). Neuroimage 142, 522–532.
- Szczepankiewicz, F., Westin, C.-F., Nilsson, M., 2019. Maxwell-compensated design of asymmetric gradient waveforms for tensor-valued diffusion encoding. Magn. Reson. Med. 82 (4), 1424–1437.
- Szczepankiewicz, F., Westin, C.-F., Nilsson, M., 2020. Gradient waveform design for tensor-valued encoding in diffusion mri. J. Neurosci. Methods 109007.
- Topgaard, D., 2017. Multidimensional diffusion mri. J. Magn. Reson. 275, 98-113.
- Tournier, J.-D., Calamante, F., Connelly, A., 2007. Robust determination of the fibre orientation distribution in diffusion MRI: non-negativity constrained super-resolved spherical deconvolution. Neuroimage 35 (4), 1459–1472.
- Tournier, J.-D., Smith, R., Raffelt, D., Tabbara, R., Dhollander, T., Pietsch, M., Christiaens, D., Jeurissen, B., Yeh, C.-H., Connelly, A., 2019. Mrtrix3: a fast, flexible and open software framework for medical image processing and visualisation. Neuroimage 116137.
- Tuch, D.S., 2004. Q-ball imaging. Magn. Reson. Med 52 (6), 1358-1372.
- Veraart, J., Novikov, D.S., Christiaens, D., Ades-Aron, B., Sijbers, J., Fieremans, E., 2016.

  Denoising of diffusion MRI using random matrix theory. Neuroimage 142, 394–406.
- Virtanen, P., Gommers, R., Oliphant, T.E., Haberland, M., Reddy, T., Cournapeau, D., Burovski, E., Peterson, P., Weckesser, W., Bright, J., et al., 2020. Scipy 1.0: fundamental algorithms for scientific computing in python. Nat. Methods 17 (3), 261–272.
- Walt, S.v.d., Colbert, S.C., Varoquaux, G., 2011. The numpy array: a structure for efficient numerical computation. Comput. Sci. Eng. 13 (2), 22–30.
- Wedeen, V.J., Wang, R., Schmahmann, J.D., Benner, T., Tseng, W.-Y.I., Dai, G., Pandya, D., Hagmann, P., D'Arceuil, H., de Crespigny, A.J., 2008. Diffusion spectrum magnetic resonance imaging (dsi) tractography of crossing fibers. Neuroimage 41 (4), 1267–1277.
- Westin, C.-F., Knutsson, H., Pasternak, O., Szczepankiewicz, F., Özarslan, E., van Westen, D., Mattisson, C., Bogren, M., O'Donnell, L.J., Kubicki, M., et al., 2016. Q-space trajectory imaging for multidimensional diffusion MRI of the human brain. Neuroimage 135, 345–362.
- Westin, C.-F., Szczepankiewicz, F., Pasternak, O., Özarslan, E., Topgaard, D., Knutsson, H., Nilsson, M., 2014. Measurement tensors in diffusion mri: generalizing the concept of diffusion encoding. In: International Conference on Medical Image Computing and Computer-Assisted Intervention. Springer, pp. 209–216.
- Yang, G., Tian, Q., Leuze, C., Wintermark, M., McNab, J.A., 2018. Double diffusion encoding MRI for the clinic. Magn. Reson. Med. 80 (2), 507–520.
- Zhang, H., Schneider, T., Wheeler-Kingshott, C.A., Alexander, D.C., 2012. Noddi: practical in vivo neurite orientation dispersion and density imaging of the human brain. Neuroimage 61 (4), 1000–1016.
- Zhou, F.-L., Li, Z., Gough, J.E., Cristinacce, P.L.H., Parker, G.J., 2018. Axon mimicking hydrophilic hollow polycaprolactone microfibres for diffusion magnetic resonance imaging. Mater. Des. 137, 394–403.